

Received:
21 February 2018
Revised:
28 May 2018
Accepted:
29 August 2018

Cite as: Syed Rahin Ahmed,
Seon Woo Kang, Sangjin Oh,
Jaebeom Lee, Suresh
Neethirajan. Chiral zirconium
quantum dots: A new class of
nanocrystals for optical
detection of coronavirus.
Heliyon 4 (2018) e00766.
doi: 10.1016/j.heliyon.2018.
e00766



Chiral zirconium quantum dots: A new class of nanocrystals for optical detection of coronavirus

Syed Rahin Ahmed ^a, Seon Woo Kang ^b, Sangjin Oh ^b, Jaebeom Lee ^b,
Suresh Neethirajan ^{a,*}

^a BioNano Laboratory, School of Engineering, University of Guelph, Guelph, Ontario N1G 2W1, Canada

^b Department of Cogno-Mechatronics Engineering, Pusan National University, Busan 609-735, Republic of Korea

*Corresponding author.

E-mail address: sneetirajan@gmail.com (S. Neethirajan).

Abstract

A synthetic way of chiral zirconium quantum dots (Zr QDs) was presented for the first time using L(+) -ascorbic acid acts as a surface as well as chiral ligands. Different spectroscopic and microscopic analysis was performed for thorough characterization of Zr QDs. As-synthesized QDs exhibited fluorescence and circular dichroism properties, and the peaks were located at 412 nm and 352 nm, respectively. MTT assay was performed to test the cytotoxicity of the synthesized Zr QDs against rat brain glioma C6 cells. Synthesized QDs was further conjugated with anti-infectious bronchitis virus (IBV) antibodies of coronavirus to form an immunolink at the presence of the target analyte and anti-IBV antibody-conjugated magneto-plasmonic nanoparticles (MPNPs). The fluorescence properties of immuno-conjugated QD–MP NPs nanohybrids through separation by an external magnetic field enabled biosensing of coronavirus with a limit of detection of 79.15 EID/50 µL.

Keywords: Nanotechnology, Materials chemistry, Materials science, Biomedical engineering

1. Introduction

Due to the exceptional optical and electrical behavior of the group II–VI elements of periodic table arising from quantum confinements of electrons and large surface area, much research has been conducted on novel nanomaterials over the last several years. Nanoscale materials, i.e., quantum dots (QDs) containing the above mentioned group elements possess a number of promising characteristics, i.e., (i) strong fluorescence emission and optical stability; (ii) broad range excitation wavelength; (iii) better quantum yield (QY); and (iv) tunable emission peak ranging from the ultraviolet to the infrared region. These exceptional properties provide tremendous potential for interdisciplinary research among nanotechnologists, bioengineers, physicists, and chemists, as well as cooperation between academic research and industrial production (Bao and Bawendi, 2015; Chen et al., 2013; Howes et al., 2014; Kershaw and Rogach, 2015).

A huge number of different QDs has been reported and extensively investigated containing the elements of II & VI group (Cho et al., 2013; de Azevedo and Menezes, 2012; Jiang et al., 2012; Koneswaran and Narayanaswamy, 2015; Liu et al., 2013; Montalti et al., 2015; Vanmaekelbergh et al., 2015; Zhang et al., 2015). Though those QDs are envisioned as a promising class of nanocrystals and have significant interest because of excellent photostability and changeable emission properties, the problems associated with cadmium-, indium-, selenium-, and arsenic-based QDs are their inherent conflicting reports on their toxicity, which has hampered their extended validation in clinical trials for use in humans (Ahmed et al., 2018; Corazzari et al., 2013; Li et al., 2009; Xu et al., 2016; Yong et al., 2013). Biocompatible and water dispersible QDs are preferred for biological applications and also due to environmental disposal requirements. Only few efforts have been made recently to prepare biocompatible QDs (Cui et al., 2009; Deng et al., 2012; Hinds et al., 2006; Ma et al., 2009; Rosenthal et al., 2011; Sturzenbaum et al., 2013; Tikhomirov et al., 2011; Zhou et al., 2011). In spite of the approaches to making biocompatible QDs, a few issues such as scalability remain to be resolved; for example, living organisms that can produce QDs has the drawback of high-throughput production. Furthermore, the functionalization of QDs with biocompatible molecules may cause a loss of quantum yield, and is also a multistep preparative process. Hence, a one-step QD synthesis process with biocompatible properties is urgently needed.

The introduction of chiral QDs' with induced optical chirality and fluorescent emission at both visible and infrared ranges would significantly benefit the development of numerous biosensing and bioimaging applications. The chirality of nanomaterials has recently been explored in modern nanoscience as an alternative to natural chiral molecules due to the former's excellent photostability, thermal stability, biocompatibility, and low toxicity. These properties open new possibilities in catalysis, chiral sensing, optical communications systems and imaging applications, and metamaterials

in advanced optical devices (Ahmed et al., 2018; Baimuratov et al., 2015; Filippone et al., 2009; Suzuki et al., 2016; Tohgha et al., 2013; Vazquez-Nakagawa et al., 2016; Yang et al., 2014; Zhu et al., 2008; Zhou et al., 2010).

Zirconium, a group IVB transition metal element, has been applied in different technological applications, for example, in catalysis, fuel cells, and the biomedical field due to its nontoxicity, ability to capture UV light capture, thermal stability, and mechanical strength. Advancement of nanotechnology has introduced Zr at the nano-scale dimension with peculiar size-dependent physical and chemical properties because of large surface area and the confinement of electronic states compared to its bulk regime (Liu et al., 2016; Puigdollers et al., 2016; Vennemann et al., 2017; Wang et al., 2016). However, despite a few studies on the synthesis and characterization of zirconium nanoparticles (Zr NPs), till date there has been no report on the synthesis of zirconium quantum dots (Zr QDs). It is expected that Zr QDs will bring new opportunities in not only in optics arena but also in other diverse research sector.

Herein, we have reported a one-step conversion of Zr NPs to chiral Zr QDs with the assistance of an autoclave. The synthesized Zr QDs showed blue fluorescence emission as well as demonstrated aqueous dispersibility, and was further applied in the biosensing of infectious bronchitis virus (IBV).

Respiratory disease in chickens caused by Infectious bronchitis virus (IBV) consisting of several physical symptoms and can replicate in the oviduct of infected birds, resulting in reduced egg production and fertility. IBV strains affects the chicken's kidneys, causing significant mortality. Most importantly, the emergence of new IBV variants every year remains a serious problem for the poultry industry and global economy (Ahmed et al., 2017; Grgić et al., 2008). Hence, IBV was chosen as a model analyte to develop a fluorescence based sensor integrated with nanotechnology for rapid detection.

2. Materials and methods

Zirconium nanoparticles, HAuCl₄.3H₂O, 3,3',5,5'-tetramethylbenzidine (TMB), 3-mercaptopropionic acid, bovine serum albumin (BSA), H₂O₂, and 96-well plates were purchased from Sigma-Aldrich (St. Louis, MO, USA). Ascorbic acid was received from Wako Pure Chemical Industries, Ltd. (Osaka, Japan). Highly pure deionized (DI) water (>18 MΩ·cm) was used in all the experiments.

2.1. Synthesis of Zr QDs

1 mL (0.1 M) solution of ascorbic acid was mixed with Zr NPs (0.5 mg/mL, 20 mL) and autoclave for 1 h at 150 °C. Then, the synthesized QD solution was kept at room temperature for cooling down.

2.2. MTT assay

To demonstrate the toxicity of Zr QDs against cells, cytotoxicity was evaluated by Methylthiazolyldiphenyl-Tetrazolium (MTT) assay in this study. C6 glioma cells (2×10^4 cells per mL) were obtained from Korean Cell Line Bank (Seoul, Korea) and was cultivated in 96-well plates. After 24 h, particles were added into the wells at a series of dilution factors. After twenty-four hours of incubation, supernatants of cells were removed, then 100 μ L of media and MTT solution (10 μ L) were added to the cell culture plate for 4 h. A total of 10% Sodium dodecyl sulfate (SDS; IBS-BS003a, Intron Biotechnology, Seongnam, Gyeonggi-do, Korea) solution (100 μ L) with 0.2% of hydrochloric acid was added to the cell culture plate and remained in the dish for 18 h.

2.3. Synthesis of spiky magnetoplasmonic nanoparticles (MP NPs)

Water-soluble MP NPs were prepared based on the previously reported method (Zhou et al., 2014). Briefly, 400 μ L solution of as-prepared smooth gold nanoparticle (Au NPs)—coated Fe_3O_4 , 1% aqueous solution of trisodium citrate (22 μ L), and hydroquinone solution (1 mL, 30 mM) were added sequentially to a HAuCl_4 solution (0.25 mM, 10 mL) for 30 min at 25 °C. Here, $\text{Fe}_3\text{O}_4@\text{Au}$ NPs core-shell structured particles served as seeds, and Au^{3+} ions were reduced on it with the addition of the hydroquinone.

2.4. The culture of IBV

The procedures of propagation and titration of virus was followed as previously described (Gelb, 1998; Grgić et al., 2008). The concentration of the stock solution was $1 \times 10^6 \text{ EID}_{50}/\text{mL}$.

2.5. Specificity of antibodies toward bronchitis virus (IBV)

The conventional ELISA was performed for the specificity of the IBV antibodies to IBV. 50 μ L ($1 \times 10^3 \text{ EID}_{50}/\text{mL}$) virus solutions were kept on polystyrene plate at 4 °C for 8h. Then, after rinsed, blocking agents was added for 1h. Then, anti-IBV Ab (1 $\mu\text{g}/\text{mL}$), anti-H5N2Ab (1 $\mu\text{g}/\text{mL}$), anti-H4 Ab (1 $\mu\text{g}/\text{ml}$), and anti-H5N1Ab (1 $\mu\text{g}/\text{mL}$) were added to the wells, incubated at 25 °C for 1 h. HRP-conjugated secondary antibody (50 μ L, 1 $\mu\text{g}/\text{mL}$) was added for 1h. At last, TMB (10 nM)/ H_2O_2 (5 nM) solution was mixed to all well (50 μ L/well) for 10 min. 10% H_2SO_4 solution (50 $\mu\text{L}/\text{well}$) was used to stop the reaction.

2.6. Conjugation of anti-IBV antibodies with Zr QDs

Electrostatic force was used to bind between IBV-specific antibodies and Zr QDs. A mixture of PLL (200 μ L) and QDs (800 μ L) was kept for 1 h at 25 °C. Zr QDs will be covered by PLL in this step. The anti-IBV antibody (1 μ g/mL) added on this solution for 1 h. Antibodies will bind with PLL at this stage. 1 ng/mL (50 μ L) of anti-mouse IgG-HRP was added to all well for 1 h. Upon adding of 100 μ L TMB solution for 20 min, blue colored solution was appeared.

2.7. Conjugation of anti-IBV antibodies and MP NPs

To bind MP NPs with antibodies, 100 μ L solution of 3-mercaptopropionic acid (MPA) (10 mM) was mixed with MP NPs (900 μ L) and gently stirred at room temperature for an hour. Then the mixture was separated through centrifugal force (4,500 rpm, 30 min) and redispersed on PBS buffer (pH 7.5, 1 mL). At this stage, the carboxylic group will be covered on the surface of MP NPs. To make a conjugation between MP NPs and anti-IBV antibodies, MP NPs (1 mL) was mixed with EDC (4 mM), NHS (10 mM) and 1 μ L anti-IBV antibodies (1 μ g/mL) for 1 h.

3. Results & discussions

In this study, we have reported a two-step way of hetero structuring magnetoplasmonic and fluorescent nanocrystals through immunoreaction for IBV detection. Firstly, ZrQDs and MP NPs were prepared, then antibodies were conjugated with nanomaterials (Fig. 1A–D). ZrQDs and MP NPs will stay apart from each other

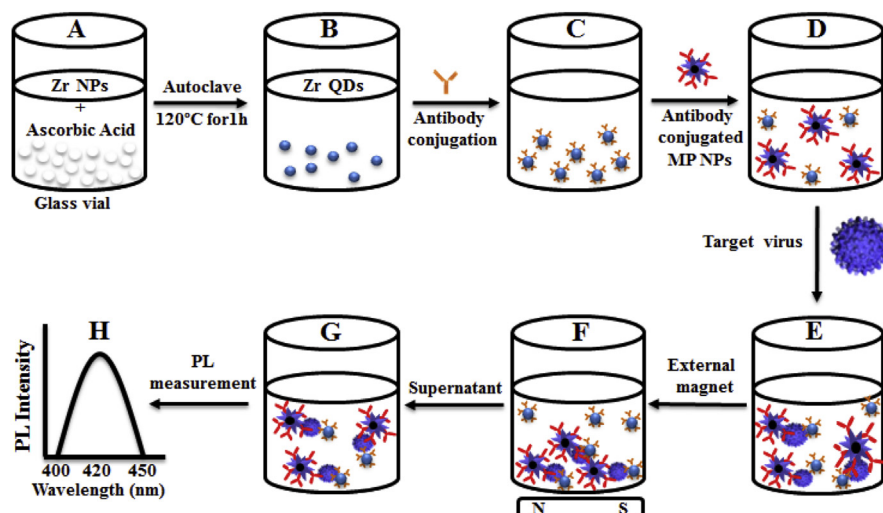


Fig. 1. Scheme of sensor design: (A) Zr nanoparticles and reducing agent keep on vial; (B) Zr QDs formation; (C) antibody conjugated QDs; (D) the addition of antibody-conjugated MP NPs; (E) formation of nanostructured magnetoplasmonic-fluorescent with the addition of target, then separated (F); (G) the nanohybrid-conjugated part was dispersed and measure the optical properties (H).

since no attraction between them at this point. Antibody-conjugated ZrQDs and MP NPs will come closer and will make a magnetoplasmonic-fluorescent nanohybrids structure while target analyte was added ([Fig. 1E](#)). Then, external magnet can be used to separate nanostructured magnetoplasmonic-fluorescent ([Fig. 1F & G](#)), and the photoluminescence (PL) intensity of nanohybrids can be used to measure the analyte's concentration ([Fig. 1H](#)).

The fluorescence and absorbance spectra of Zr QDs were appeared at 412 nm and 378 nm, respectively ([Fig. 2A & B](#)). As-prepared Zr QDs showed chiral peak at 352 nm ([Fig. 2C](#)). Zr QDs showed light yellow color at daylight, and blue under UV-light ([Fig. 2D](#)).

The quantum yield value of the synthesized Zr QDs was 9.16 % and the fluorescence lifetime was 1.92 ns.

Zr QDs synthetic route was shown in [Fig. 3A](#). After synthesis of Zr QDs, FEI Titan 8-300 TEM machine was used to take HRTEM of Zr NPs and QDs. As shown in [Fig. 3B](#), the Zr NPs were approximately 15–20 nm in size. A far image of as Zr QDs showed that the QDs size was 2–3 nm ([Fig. 3C](#)). HRTEM image revealed Zr QDs contained lattice spacing of 0.2821 nm, indicating (100) lattice planes of the Zr ([Fig. 3D](#)) ([Almyras et al., 2010](#)).

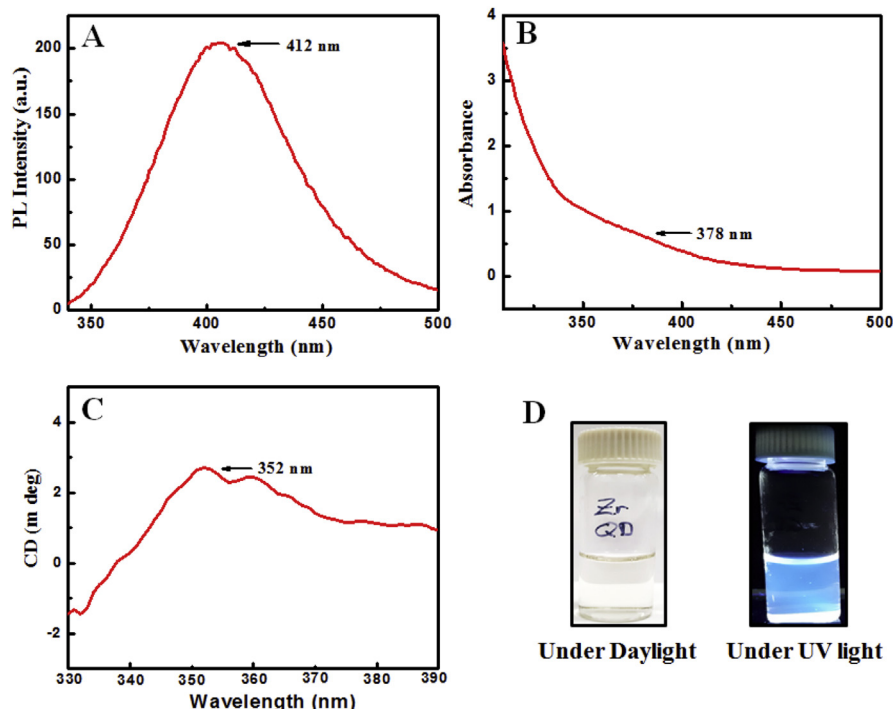


Fig. 2. Optical properties of Zr QDs: (A) PL intensity and absorbance spectra of Zr QDs (B); (C) chiral spectra and (D) color of solution.

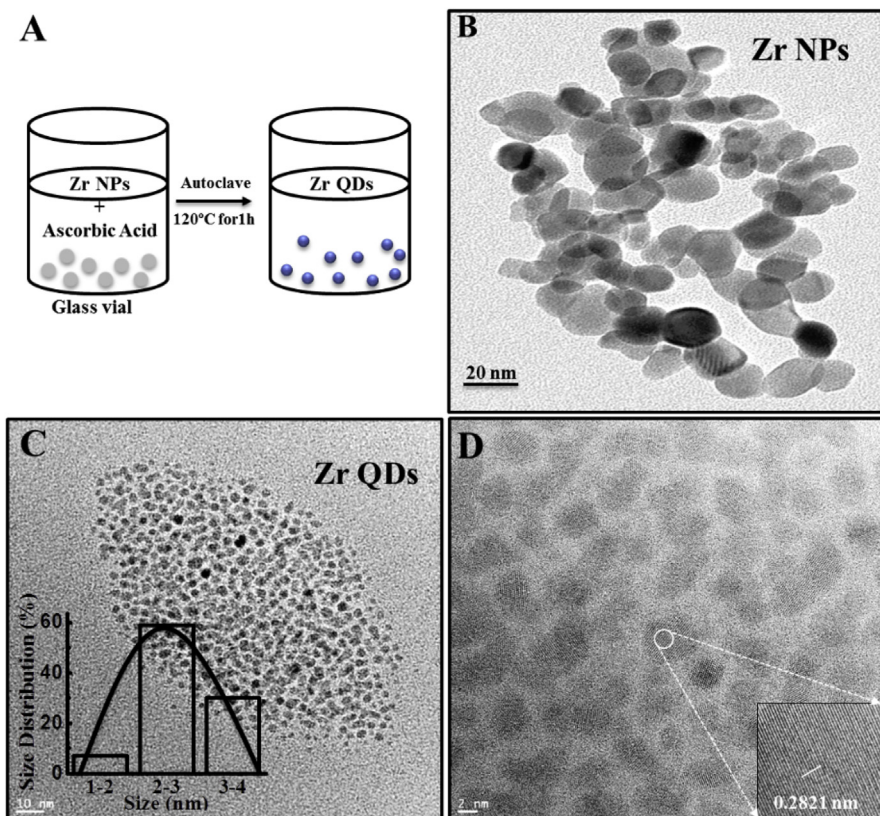


Fig. 3. Image of Zr QDs and Zr NPs: (A) Scheme of Zr QD synthesis; (B) HRTEM image of ZrNPs and QDs (C) (inset: size distribution profile); (D) HRTEM image of Zr QDs (inset: lattice pattern of ZrQDs).

Fig. 4 shows the XPS spectrum of Zr NPs (**Fig. 4A**) and QDs (**Fig. 4B**). A peak of Zr $3d_{3/2}$ and Zr $3d_{5/2}$ were appeared in all the samples. In Zr NPs, the Zr 3d peaks were observed at 185.4 eV for $3d_{5/2}$ and 187.7 eV for $3d_{3/2}$, as shown in **Fig. 4A** (Ali et al., 2014; Bakradze et al., 2011; Ma et al., 2015). However, the peaks of Zr $3d_{3/2}$ and Zr $3d_{5/2}$ were slightly shifted for Zr QDs, probably due to the change and coupling of electronic state.

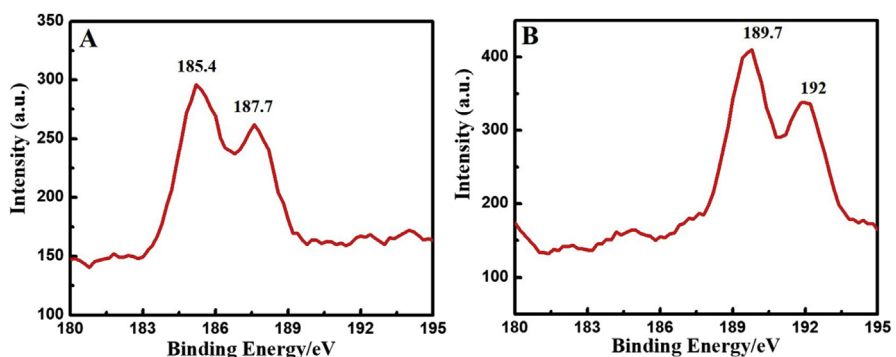


Fig. 4. XPS data of Zr NPs (A) and Zr QDs (B).

The crystallinity of Zr QDs was analyzed by XRD spectroscopy and shown in Fig. 5. It is clear from Fig. 3 that as-synthesized Zr QDs contain two crystalline phases: a monoclinic phase, marked with the red squares, and a tetragonal phase, marked with the blue squares. Zr QDs contain a higher component of the monoclinic than the tetragonal phase. The peak positions of Zr QDs and ZrO₂ are shifted a little bit (Ali et al., 2014; Eshed et al., 2011), probably, due to the crystal defects formed during synthesis.

The cytotoxicity of as-prepared Zr QDs was performed on C6 glioma cells using MTT assay. As shown in Fig. 6, no obvious cytotoxicity effects on C6 glioma cells

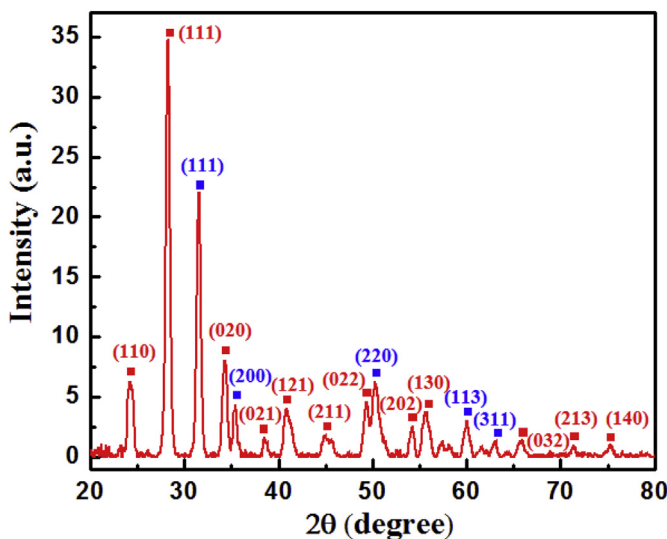


Fig. 5. X-ray diffraction (XRD) spectra of synthesized Zr QDs.

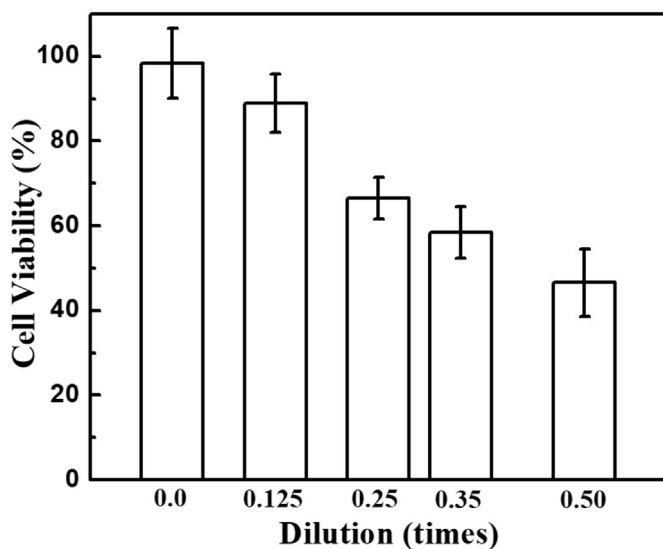


Fig. 6. Cell viability study of Zr QDs.

was observed with 0.125 times dilution of Zr QDs compared with the control group. In this study, we performed the nanotoxicity effects of Zr QDs without surface modification. Insightful cytotoxicity study of as-prepared Zr QDs may be needed with surface modification with different biomolecules and their application on different cells in near future.

Transmission electron microscopy (TEM) images of spiky magneto-plasmonic nanoparticles are shown in Fig. 7A. The average size of particles was around 50 nm. Magnified close-up TEM image showed the surface of the MP NPs containing spiky tips of approximately 10 nm in size (Fig. 7B). Naked eye color of solution was showed at the inset of Fig. 7B. The broadened plasmonic peak of the MP NPs was located at 598 nm (Fig. 7C). The SQUID measurement of MP NPs has shown in Fig. 7D. The magnetic saturation value of MP NPs observed at 60.0 emug^{-1} .

The specificity of anti-IBV antibodies toward the target IBV was shown in Fig. 8. A higher absorbance value of anti-IBV antibodies in comparison to others tells that anti-IBV antibodies have a strong binding affinity toward the target IBV.

Anti-IBV antibodies binding with MP NPs and Zr QDs was shown Fig. 9. A higher absorbance value for anti-IBV antibodies with nanomaterials indicates the confirmation

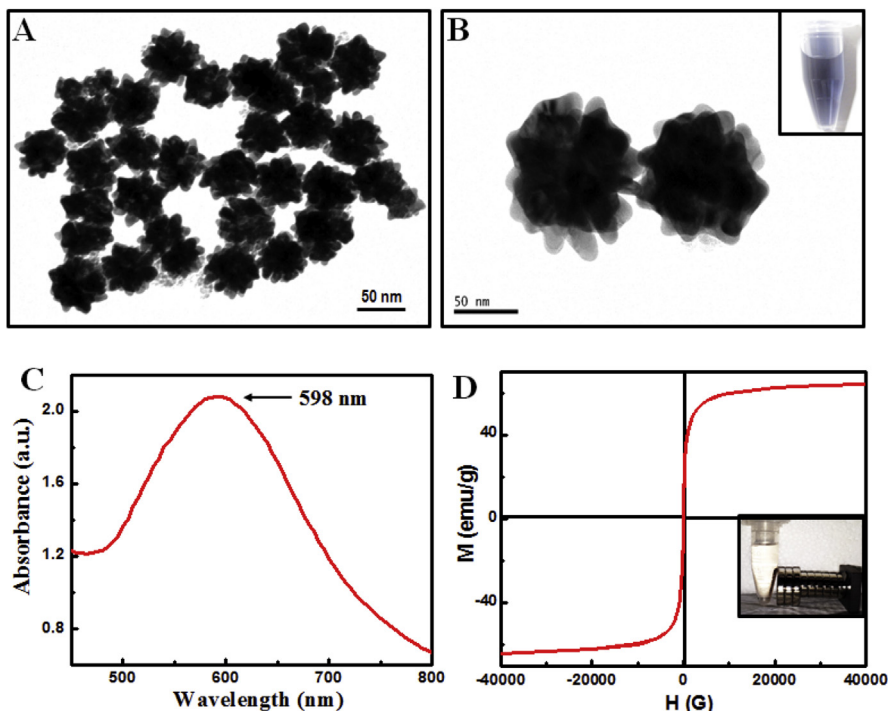


Fig. 7. Characterization of MP NPs: (A) Large-scale TEM image of MP NPs; (B) close-up view of MP NPs (inset: color of solution); (C) the absorbance spectra of MP NPs; and (D) the SQUID measurement of MP NPs.

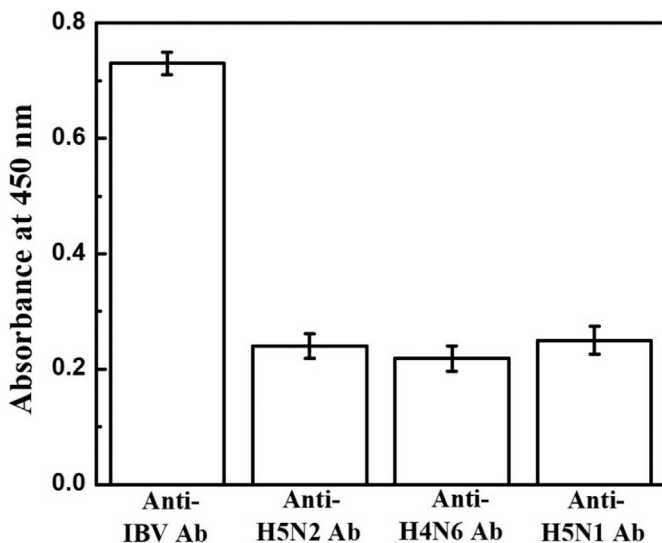


Fig. 8. The specificity of anti-IBV antibodies for coronavirus.

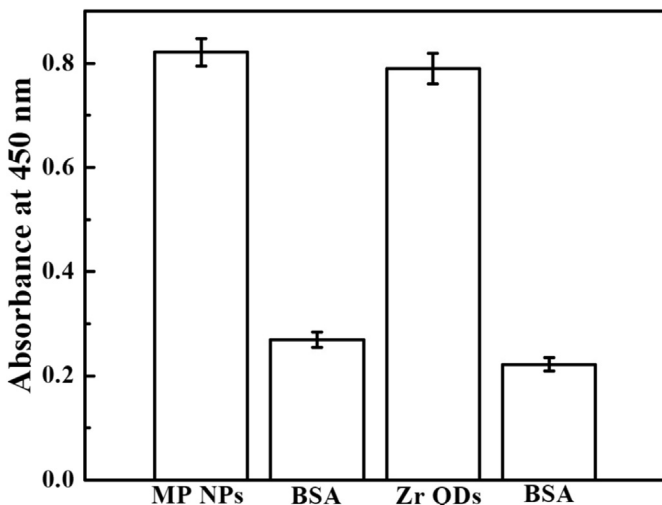


Fig. 9. The conjugation of antibodies with nanomaterials.

of binding between antibodies and nanomaterials. Also, the change of zeta potential value further supported the conjugation of antibodies with QDs ([Table 1](#)).

FTIR spectrum analyzed for the amide bond formation between antibodies and MP ([Fig. 10](#)). The peak at $3500\text{--}3700\text{ cm}^{-1}$ and $1630\text{--}1690\text{ cm}^{-1}$ corresponds the N–H stretching and C=O stretching of amide bond respectively.

Table 1. Step by step analysis of zeta potential value.

Zeta potential (mV)		
Zr QDs	After conjugation with Poly-L-lysine (PLL)	After conjugation with antibodies
-13.32	+8.07	-1.97

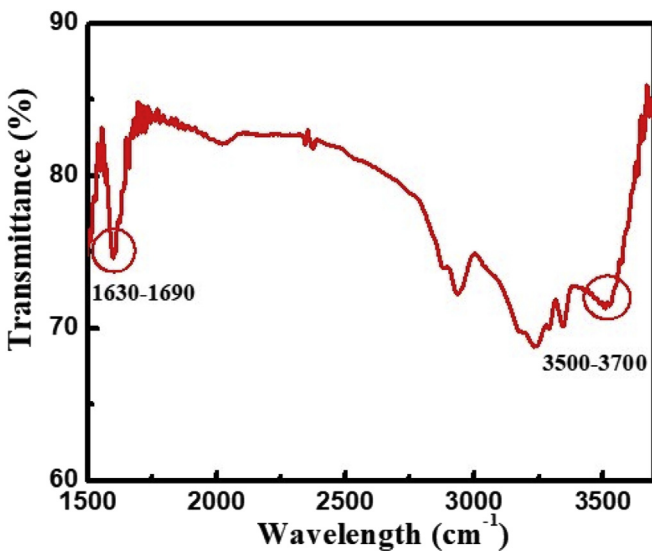


Fig. 10. FTIR spectra of MP NPs and anti-IBV antibodies binding.

The fluorescence intensity of immune-linked magnetoplasmonic-fluorescent nano-hybrids increased approximately 25% in comparison to antibody-conjugated Zr QDs (Fig. 11A). The change in fluorescence intensity at different concentrated virus solution was investigated (Fig. 11B and C). The PL intensity changes with the different concentrations of virus solution was linearly responds in the range of 10,000 EID/50 μL to 100 EID/50 μL with an LOD value of 79.15 EID/50 μL .

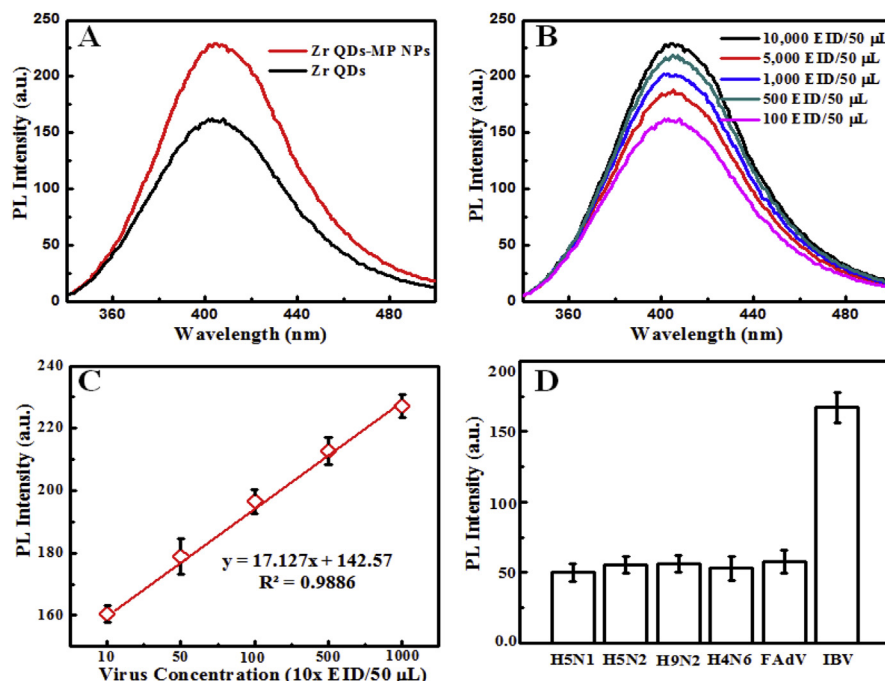


Fig. 11. Fluorescence-based detection of IBV: (A) PL intensity responses; (B) Target virus concentration dependent PL intensity; (C) PL intensity Vs virus concentration curve; and (D) selectivity test.

Table 2. A comparison study of IBV detection.

Method	Concentration (EID/50 µL)						
	10000	5000	1000	500	100	50	10
This study	+	+	+	+	+	-	-
Conventional ELISA	+	+	+	-	-	-	-

The selectivity of the proposed bioassay was examined with other virus strains, namely H5N1, H5N2, H9N2, H4N6, and FAdV. A significant difference of fluorescence intensity was observed with the target IBV compare to others, indicating that the proposed assay is highly selective for the target analyte (Fig. 11D).

The sensitivity of this assay was compared with the ELISA method (Table 2). The colorimetric response of IBV using ELISA was 1000 EID/50 µL, tells us that the proposed fluorescence assay is 10 times more sensitive than ELISA.

In this study, we have introduced aqueous soluble chiral Zr QDs for the first time. There is still much to be learned about the nature of Zr QDs, such as how excitonic properties arise on it, it's size-tunable optical properties, surface modification with different biological molecules, and the control of the interaction between Zr QDs and plasmonic metals.

4. Conclusions

Here, we have presented a new nanocrystal synthesis method—i.e., Zr QDs—and a series of characterizations was performed to check the nanocrystals' optical properties, morphology, and practicability in biological applications. Furthermore, a bioassay was proposed to achieve enhanced sensitivity for IBV detection using as-prepared Zr QDs and MP NPs in blood media, which showed greater sensitivity than conventional ELISA methods. Most importantly, the introduction of novel QDs synthesis and an optical-based bioassay may open new doors for research and further optical applications.

Declarations

Author contribution statement

Syed Rahin Ahmed: Performed the experiments; Analyzed and interpreted the data; Wrote the paper.

Seon Woo Kang: Performed the experiments.

Sangjin Oh: Performed the experiments; Contributed reagents, materials, analysis tools or data.

Jaebeom Lee, Suresh Neethirajan: Conceived and designed the experiments; Contributed reagents, materials, analysis tools or data.

Funding statement

This work was supported by the Natural Sciences and Engineering Research Council of Canada (400705) and the National Research Foundation of Korea (NRF) Grant funded by the Korean Government (MSIP) (2016R1A2B4012072, 2017R1A4A1015627).

Competing interest statement

The authors declare no conflict of interest.

Additional information

No additional information is available for this paper.

Acknowledgements

The authors thank the Natural Sciences and Engineering Research Council of Canada and the Ontario Ministry of Agriculture, Food and Rural Affairs for funding this study. We express our strong acknowledgements to Prof. Rod Merrill of the Molecular and Cell Biology department of the University of Guelph for give us access of circular dichroism equipment.

References

- Ahmed, S.R., Nagy, É., Neethirajan, S., 2017. Self-assembled star-shaped chiroplasmonic gold nanoparticles for an ultrasensitive chiro-immunosensor for viruses. *RSC Adv.* 7, 40849–40857.
- Ahmed, S.R., Mogus, J., Chand, R., Nagy, É., Neethirajan, S., 2018. Optoelectronic fowl adenovirus detection based on local electric field enhancement on graphene quantum dots and gold nanobundle hybrid. *Biosens. Bioelectron.* 103, 45–53.
- Ali, G., Park, Y.J., Kim, H.J., Cho, S.O., 2014. Formation of self-organized Zircaloy-4 oxide nanotubes in organic viscous electrolyte via anodization. *Nanoscale Res. Lett.* 9, 553.

- Almyras, G.A., Matenoglou, G.M., Komninou, P., Kosmidis, C., Patsalas, P., Evangelakis, G.A., 2010. On the deposition mechanisms and the formation of glassy Cu–Zr thin films. *J. Appl. Phys.* 107, 084313.
- Baimuratov, A.S., Rukhlenko, I.D., Noskov, R.E., Ginzburg, P., Gu’no, Y.K., Baranov, A.V., Fedorov, A.V., 2015. Giant optical activity of quantum dots, rods, and disks with screw dislocations. *Sci. Rep.* 5, 14712.
- Bakradze, G., Jeurgens, L.P.H., Mittemeijer, E.J., 2011. Valence-band and chemical-state analyses of Zr and O in thermally grown thin zirconium-oxide films: an XPS study. *J. Phys. Chem. C* 115, 19841–19848.
- Bao, J., Bawendi, M.G., 2015. A colloidal quantum dot spectrometer. *Nature* 523, 67–70.
- Chen, O., Zhao, J., Chauhan, V.P., Cui, J., Wong, C., Harris, D.K., Wei, H., Han, H.S., Fukumura, D., Jain, R.K., Bawendi, M.G., 2013. Compact high-quality CdSe–CdS core–shell nanocrystals with narrow emission linewidths and suppressed blinking. *Nat. Mater.* 12, 445–451.
- Cho, E., Jang, H., Lee, J., Jang, E., 2013. Modeling on the size dependent properties of InP quantum dots: a hybrid functional study. *Nanotechnology* 24, 215201–215201.
- Corazzari, I., Gilardino, A., Dalmazzo, S., Fubini, B., Lovisolo, D., 2013. Localization of CdSe/ZnS quantum dots in the lysosomal acidic compartment of cultured neurons and its impact on viability: potential role of ion release. *Toxicol. Vitro* 27, 752–759.
- Cui, R., Liu, H.H., Xie, H.Y., Zhang, Z.L., Yang, Y.R., Pang, D.W., Xie, Z.X., Chen, B.B., Hu, B., Shen, P., 2009. Living yeast cells as a controllable bio-synthesizer for fluorescent quantum dots. *Adv. Funct. Mater.* 19, 2359–2364.
- de Azevedo, W.M., Menezes, F.D., 2012. A new and straightforward synthesis route for preparing Cds quantum dots. *JOL* 132, 1740–1743.
- Deng, Z.T., Samanta, A., Nangreave, J., Yan, H., Liu, Y., 2012. Robust DNA-functionalized core/shell quantum dots with fluorescent emission spanning from UV–vis to near-IR and compatible with DNA-directed self-assembly. *J. Am. Chem. Soc.* 134, 17424–17427.
- Eshed, M., Pol, S., Gedanken, A., Balasubramanian, M., 2011. Zirconium nanoparticles prepared by the reduction of zirconium oxide using the RAPET method. *Beilstein J. Nanotechnol.* 2, 198–203.
- Filippone, S., Maroto, E.E., Martin-Domenech, Á., Suarez, M., Martin, N., 2009. An efficient approach to chiral fullerene derivatives by catalytic enantioselective 1, 3-dipolar cycloadditions. *Nat. Chem.* 1, 578–582.

- Gelb, J.J., 1998. The American Association of Avian Pathologists, fourth ed. Kendall/Hunt Publ, Dubuque, Iowa, pp. 69–175.
- Grgić, H., Hunter, D.B., Hunton, P., Nagy, É., 2008. Pathogenicity of infectious bronchitis virus isolates from Ontario chickens. *Can. J. Vet. Res.* 72, 403–410.
- Hinds, S., Taft, B.J., Levina, L., Sukhovatkin, V., Dooley, C.J., Roy, M.D., MacNeil, D.D., Sargent, E.H., Kelley, S.O., 2006. Nucleotide-directed growth of semiconductor nanocrystals. *J. Am. Chem. Soc.* 128, 64–65.
- Howes, P.D., Chandrawati, R., Stevens, M.M., 2014. Colloidal nanoparticles as advanced biological sensors. *Science* 346, 1247390.
- Jiang, P., Zhu, C.-N., Zhang, Z.-L., Tianand, Z.-Q., Pang, D.-W., 2012. Water-soluble Ag₂S quantum dots for near-infrared fluorescence imaging in vivo. *Biomaterials* 33, 5130–5135.
- Kershaw, S.V., Rogach, A.L., 2015. Infrared emitting HgTe quantum dots and their waveguide and optoelectronic devices. *J. Phys. Chem.* 229, 23–64.
- Koneswaran, M., Narayanaswamy, R., 2015. Ultrasensitive detection of vitamin B6 using functionalised CdS/ZnS core–shell quantum dots. *Sens. Actuators B Chem.* 210, 811–816.
- Li, K.G., Chen, J.T., Bai, S.S., Wen, X., Song, S.Y., Yu, Q., Li, J., Wang, Y.Q., 2009. Intracellular oxidative stress and cadmium ions release induce cytotoxicity of unmodified cadmium sulfide quantum dots. *Toxicol. Vitro* 23, 1007–1013.
- Liu, Q., Guo, B., Rao, Z., Zhang, B., Gong, J.R., 2013. Strong two-photon-induced fluorescence from photostable, biocompatible nitrogen-doped graphene quantum dots for cellular and deep-tissue imaging. *Nano Lett.* 13, 2436–2441.
- Liu, C., Hajagos, T.J., Chen, D., Chen, Y., Kishpaugh, D., Pei, Q., 2016. Efficient one-pot synthesis of colloidal zirconium oxide nanoparticles for high-refractive-index nanocomposites. *ACS Appl. Mater. Interfaces* 8, 4795–4802.
- Ma, N., Sargent, E.H., Kelley, S.O., 2009. Non-equilibrium oxidation states of zirconium during early stages of metal oxidation. *Nat. Nanotechnol.* 4, 121–125.
- Ma, W., Herbert, F.W., Senanayake, S.D., Yildiz, B., 2015. Non-equilibrium oxidation states of zirconium during early stages of metal oxidation. *Appl. Phys. Lett.* 106, 101603.
- Montalti, M., Cantelli, A., Battistelli, G., 2015. Nanodiamonds and silicon quantum dots: ultrastable and biocompatible luminescent nanoprobes for long-term bio-imaging. *Chem. Soc. Rev.* 44, 4853–4921.

- Puigdollers, A.R., Illasand, F., Pacchioni, G., 2016. Structure and properties of zirconia nanoparticles from density functional theory calculations. *J. Phys. Chem. C* 120, 4392–4402.
- Rosenthal, S.J., Chang, J.C., Kovtun, O., McBride, J.R., Tomlinson, I.D., 2011. Biocompatible quantum dots for biological applications. *Chem. Biol.* 18, 10–24.
- Sturzenbaum, S.R., Hockner, M., Panneerselvam, A., Levitt, J., Bouillard, J.S., Taniguchi, S., Dailey, L.A., Khanbeigi, R.A., Rosca, E.V., Thanou, M., 2013. Biosynthesis of luminescent quantum dots in an earthworm. *Nat. Nanotechnol.* 8, 57–60.
- Suzuki, N., Wang, Y., Elvati, P., Qu, Z., Kim, K., Jiang, S., Baumeister, E., Lee, J., Yeom, B., Bahng, J.H., Lee, J., Violand, A., Kotov, N.A., 2016. Chiral graphene quantum dots. *ACS Nano* 10, 1744–1755.
- Tikhomirov, G., Hoogland, S., Lee, P.E., Fischer, A., Sargent, E.H., Kelley, S.O., 2011. DNA-based programming of quantum dot valency, self-assembly and luminescence. *Nat. Nanotechnol.* 6, 485–490.
- Tohgha, U., Deol, K.K., Porter, A.G., Bartko, S.G., Choi, J.K., Leonard, B.M., Varga, K., Kubelka, J., Muller, G., Balaz, M., 2013. Ligand induced circular dichroism and circularly polarized luminescence in CdSe quantum dots. *ACS Nano* 7, 11094–11102.
- Vanmaekelbergh, D.I., Van Vugt, L.K., Bakker, H.E., Rabouw, F.T., Nijs, B.D., van Dijk-Moes, R.J., van Huis, M.A., Baesjou, P.J., van Blaaderen, A., 2015. Ligand induced circular dichroism and circularly polarized luminescence in CdSe quantum dots. *ACS Nano* 9, 3942–3950.
- Vazquez-Nakagawa, M., Rodriguez-Perez, L., Herranz, M.A., Martin, N., 2016. Chirality transfer from graphene quantum dots. *Chem. Commun.* 52, 665–668.
- Vennemann, A., Alessandrini, F., Wiemann, M., 2017. Differential effects of surface-functionalized zirconium oxide nanoparticles on alveolar macrophages, rat lung, and a mouse allergy model. *Nanomaterials* 7, 280.
- Wang, J., Yin, W., He, X., Wang, Q., Guo, M., Chen, S., 2016. Good biocompatibility and sintering properties of zirconia nanoparticles synthesized via vapor-phase hydrolysis. *Sci. Rep.* 6, 35020.
- Xu, G., Zeng, S., Zhang, B., Swihart, M.T., Yong, K., Prasad, P.N., 2016. Luminescent colloidal dispersion of silicon quantum dots from microwave plasma synthesis: exploring the photoluminescence behavior across the visible spectrum. *Chem. Rev.* 116, 12234–12327.

- Yang, F., Wang, X., Zhang, D., Yang, J., Luo, D., Xu, Z., Wei, J., Wang, J.Q., Xu, Z., Peng, F., Li, X., Li, R., Li, Y., Li, M., Bai, X., Ding, F., Li, Y., 2014. Chirality-specific growth of single-walled carbon nanotubes on solid alloy catalysts. *Nature* 510, 522–524.
- Yong, K.-T., Law, W.-C., Hu, R., Ye, L., Liu, L., Swihart, M.T., Prasad, P.N., 2013. Nanotoxicity assessment of quantum dots: from cellular to primate studies. *Chem. Soc. Rev.* 42, 1236–1250.
- Zhang, B., Wang, Y., Yang, C., Hu, S., Gao, Y., Zhang, Y., Wang, Y., Demir, H.V., Liu, L., Yong, K.-T., 2015. The composition effect on the optical properties of aqueous synthesized Cu–In–S and Zn–Cu–In–S quantum dot nanocrystals. *Phys. Chem. Chem. Phys.* 17, 25133–25141.
- Zhou, Y., Yang, M., Sun, K., Tang, Z., Kotov, N.A., 2010. Similar topological origin of chiral centers in organic and nanoscale inorganic structures: effect of stabilizer chirality on optical isomerism and growth of CdTe nanocrystals. *J. Am. Chem. Soc.* 132, 6006–6013.
- Zhou, Y., Zhu, Z., Huang, W., Liu, W., Wu, S., Liu, X., Yan Gao, Y., Tang, Z.Y., 2011. Optical coupling between chiral biomolecules and semiconductor nanoparticles: size-dependent circular dichroism absorption. *Angew. Chem. Int. Ed.* 50, 11456–11459.
- Zhou, H., Kim, J., Bahng, J.H., Kotov, N.A., Lee, J., 2014. Self-assembly mechanism of spiky magnetoplasmonic supraparticles. *Adv. Funct. Mater.* 24, 1439–1448.
- Zhu, J., Peng, H., Marshall, A.F., Barnett, D.M., Nix, W.D., Cui, Y., 2008. Formation of chiral branched nanowires by the Eshelby Twist. *Nat. Nano* 3, 477–481.